MATERIALS CHEMISTRY FRONTIERS

CHINESE CHEMICAL SOCIETY

ROYAL SOCIETY OF CHEMISTRY

RESEARCH ARTICLE

View Article Online
View Journal | View Issue

Cite this: *Mater. Chem. Front.*, 2022, **6**, 1056

Design of $NiCo_2O_4$@$NiMoO_4$ core–shell nanoarrays on nickel foam to explore the application in both energy storage and electrocatalysis†

Ya'nan Meng,[a] Jiaqi Liu,[a] Deyang Yu,[a] Chunli Guo,[a] Liangyu Liu,[a] Yingjie Hua,[b] Chongtai Wang,*[b] Xudong Zhao*[a] and Xiaoyang Liu *[ab]

$NiCo_2O_4$@$NiMoO_4$ core–shell nanowires (NCNMW) and nanosheets (NCNMS) with high electrochemical capabilities were synthesized using a simple two-step hydrothermal reaction, together with a calcination process. As active electrode materials, all of the prepared electrodes were tested in a three-electrode system. Among all the electrodes, NCNMS-2 exhibited a large specific capacity (1770.95 C g^{-1} at a current density of 3 mA cm^{-2}), a high-rate capability (1334.18 C g^{-1} at 40 mA cm^{-2}), and superior cycling stability (102.78% capability retention after 5000 cycles at 10 mA cm^{-2}). The NCNMS-2// activated carbon battery–supercapacitor hybrid device yielded a high energy density of 30.57 W h kg^{-1} at a power density of 676.06 W kg^{-1} and excellent stability with a capacitance retention of 92.71% after 5000 continuous cycles at a current density of 10 mA cm^{-2}. In addition, as an electrocatalyst for the oxygen evolution reaction (OER), the NCNMS-2 exhibited a small Tafel slope of 59 mV Dec^{-1}, and a low overpotential of 175 mV at a current density of 10 mA cm^{-2}. The excellent electrochemical performance of the hierarchical $NiCo_2O_4$@$NiMoO_4$ structure was attributed to its porosity and the characteristics of the 3D nanostructure subunits that possess many active reaction sites, rapid electron/ion transport, and high stability. Based on the excellent electrochemical properties, it will serve well for energy storage and conversion.

Received 19th November 2021,
Accepted 26th February 2022

DOI: 10.1039/d1qm01534f

rsc.li/frontiers-materials

1. Introduction

With the rapid developments in science and technology, efficient energy storage and conversion devices with environmentally benign features and low cost have become in high demand. Specifically, supercapacitors and electro-catalytic water splitting have attracted great attention in recent years.[1–4] However, the low energy density of supercapacitors (SCs) and the high-cost electrocatalysts for the oxygen evolution reaction (OER) restrict their further development.[5–7] Currently, a novel type of supercapacitor device includes the battery–supercapacitor hybrid (BSH) device, which consists of a battery type electrode and a capacitive electrode (such as carbon materials).[8] The electrochemical performances of BSHs and OER are strongly correlated with the exploration and rational design of electrode materials.[9–11] Therefore, to further enhance these electrochemical properties of the energy storage and conversion devices, a variety of novel electrode materials with high electrochemical properties must be designed and fabricated.

Recently, due to the rich transition metal resources on the earth, transition metal oxides and phosphates have attracted extensive research interest.[12] Among them, transition metal oxides with the spinel and metal–organic framework (MOF) structures have been widely studied.[13–16] Among the various oxides, bimetallic transition-metal oxides (BTMOs) have been used widely in supercapacitors as positive electrodes and in electrocatalysis owing to their low-cost, environment friendliness, rich redox reaction capabilities, and high stability.[17–21] The complex chemical compositions and synergetic effects of the transition metals can enhance the electrochemical properties of the prepared electrodes, further improving the exceptionally high specific capacitance of BSH devices. Meanwhile, BTMOs with a spinel structure consist of multiple valences for the cations, which helps optimize the electrochemical behavior of the electrocatalysts for the oxygen evolution

[a] State Key Laboratory of Inorganic Synthesis and Preparative Chemistry, College of Chemistry, Jilin University, Changchun 130012, China. E-mail: liuxy@jlu.edu.cn; Fax: +86-431-85168316; Tel: +86-431-85168316

[b] Key Laboratory of Electrochemical Energy Storage and Energy Conversion of Hainan Province, School of Chemistry and Chemical Engineering, Hainan Normal University, Haikou 571158, China

† Electronic supplementary information (ESI) available. See DOI: 10.1039/d1qm01534f

reaction (OER).[22–24] In addition, the electrical conductivity of BTMOs is usually higher than those of single transition-metal oxides (STMOs, such as Co_3O_4[25]), which contributes to the relatively low activation energy for electron transfer between metal cations.[17,26] Cobalt-based metal oxides and molybdenum-based metal oxides have been widely used in BSH devices, such as $ZnCo_2O_4$,[27,28] $CuCo_2O_4$,[29,30] $NiMoO_4$,[31,32] Ni–Co oxides[33–35] and $CoMoO_4$.[36,37] Meanwhile, BTMO and STMO materials such as $NiCo_2O_4$ and MnO_2 have been studied as catalysts.[38,39]

In addition, the electrochemical properties of the energy storage/conversion devices are not only related to the composition of the electrode materials, but also to the architectural design of the BTMO-based electrodes. Various nanostructured composites with numerous electrochemical active sites have been investigated, which can lead to faster diffusion of electrolyte ions and improved structural and electrochemical stabilities. For example, phosphorus-doped $NiCo_2O_4$ nanowires exhibit a high-specific capacity of 2747.8 F g^{-1} at a current density of 1 A g^{-1} and a prominent rate performance (maintaining 50% at 100 A g^{-1}), with excellent OER properties (300 mV at 10 mA cm^{-2}).[38] $ZnCo_2O_4$ nanosheets displayed a specific capacitance of 5100 μF cm^{-2} at a current density of 0.2 A m^{-2}, and 95% capacitance retention over 1000 cycles, with excellent OER properties of 340 mV at 10 mA cm^{-2}.[28]

The reported oxide materials usually form a monolayer structure. However, a 3D core–shell nanostructure material on Ni foams may provide a unique set of physical and chemical properties with special nanostructures, high specific surface areas, and more abundant active sites for high-performance BSH devices and efficient oxygen electrocatalysis.

Herein, we report a simple and cost-effective strategy to design and synthesize $NiMoO_4$ nanosheets (shell) coated onto $NiCo_2O_4$ nanowire arrays or nanosheet arrays (core), which were grown *in situ* on the surface of Ni foams (NFs). This unique 3D hierarchical core–shell architecture provides several advantages for enhancing electrochemical properties and oxygen electrocatalysis performance. First, the core–shell nanostructures were directly grown on the surface of NFs, without any binder additives, which could ensure high mechanical stability and electric conductivity. Second, this structure made full use of both the core and shell materials by increasing the accumulation of charge and accelerating the transportation of electrons and electrolyte ions. Third, the core–shell nanostructure materials with a more porous structure can exhibit high specific surface area and provide more active sites for a redox reaction. In addition, this structure can shorten ion diffusion paths and accelerate the penetration of the electrolyte. Due to the above reasons, materials with the core–shell structure can exhibit excellent electrochemical properties.

As expected, the prepared NCNMS-2 electrode exhibited a large specific capacity (1770.95 C g^{-1} at a current density of 3 mA cm^{-2}), a high-rate capability (1334.18 C g^{-1} at 40 mA cm^{-2}), and superior cycling stability (102.78% capability retention after 5000 cycles at 10 mA cm^{-2}). The as-assembled NCNMS-2//activated carbon BSH device yielded a high energy density of 30.57 W h kg^{-1} at the power density of 676.06 W kg^{-1} and excellent stability with a capacitance retention of 92.71% after 5000 continuous cycles at a current density of 10 mA cm^{-2}. In addition, due to the unique core–shell structure, the prepared electrodes demonstrated a superior electrocatalytic OER performance. As such, it is a promising candidate for the applications of energy conversion and storage.

2. Experimental section

2.1 Synthesis of NC-NW arrays on 3D Ni foams (NFs)

In this work, all of the chemicals were of analytical grade and used without further purification. In each synthesis, 0.291 g $Ni(NO_3)_2{\cdot}6H_2O$ (nickel nitrate hexahydrate), 0.582 g $Co(NO_3)_2{\cdot}6H_2O$ (cobalt nitrate hexahydrate), 0.074 g NH_4F (ammonium fluoride), and 0.301 g $CO(NH_2)_2$ (urea) were dissolved in 60 mL deionized water (DIW), and stirred for at least 30 min. Next, 15 mL of this solution was transferred into a 25 mL Teflon-lined stainless autoclave, followed by addition of the treated NFs (the process of cleaning NFs is described in detail in the ESI†) into the reaction solution. After the reaction took place for 4 h at 120 °C, the autoclaves were cooled down to room temperature naturally. Subsequently, the Ni–Co precursor was taken out and washed by both DIW and absolute ethanol in an ultrasonic bath, followed by drying at 60 °C for at least 12 h. Finally, the sample was annealed at 450 °C for 2 h under an air atmosphere to form the final structure of the $NiCo_2O_4$ nanowire arrays (hereinafter referred to as NC-NW).

2.2 Synthesis of NC-NS arrays on 3D Ni foam

To fabricate $NiCo_2O_4$ nanosheets (hereinafter referred to as NC-NS), 0.145 g $Ni(NO_3)_2{\cdot}6H_2O$, 0.291 g $Co(NO_3)_2{\cdot}6H_2O$, 0.093 g NH_4F, and 0.301 g $CO(NH_2)_2$ were dissolved in 30 mL DIW and then stirred for 10 min. After the chemicals were all dissolved, 30 mL absolute ethanol was added to the mixed solution and then stirred for at least 30 min. After that step, the prepared solution and NFs were transferred into the autoclave. The autoclave was maintained at 120 °C for 4 h. After cooling down to room temperature, the samples were taken out, washed and calcined as described above.

2.3 Synthesis of NCNMW and NCNMS arrays on 3D Ni foam

NCNMW and NCNMS were synthesized *via* a second hydrothermal process. The prepared Ni–Co precursors with different morphologies together with the mixed solution containing 30 mL DIW of 0.416 g $Ni(NO_3)_2{\cdot}6H_2O$ and 0.346 g $Na_2MoO_4{\cdot}2H_2O$ (sodium molybdate dihydrate) were placed into a 25 mL Teflon-lined stainless autoclave to synthesize $NiCo_2O_4$@$NiMoO_4$ core–shell hierarchical nanostructures. The autoclaves were kept at 90 °C for 2 h and cooled down to room temperature, yielding the samples named NCNMW-2 and NCNMS-2. In parallel, when the autoclaves were kept at 90 °C for 1 h or 3 h, the yielded products were labelled as NCNMW-1, NCNMW-3 and NCNMS-1, NCNMS-3, respectively.

2.4 Characterization

Energy-dispersive X-ray (EDX) mapping and scanning electron microscopy (SEM) were recorded on a JSM-7800F, JEOL, to map the distribution of elements and to test the morphology structures and the size of the samples, respectively. The crystalline features and composition of the samples were tested by X-ray diffraction (XRD, D/max, 2550V, Cu Kα radiation) in the range of 2θ from 20° to 80°. Transmission electron microscopy (TEM) and high-resolution transmission electron microscopy (HRTEM) images were obtained by using a FEI Tecnai G2 F20 s-twin D 573. Meanwhile, X-ray photoelectron spectroscopy (XPS, ESCALAB 250, Mg Kα radiation) was used to characterize the elemental composition and chemical status of the samples.

2.5 Electrochemical measurements

Electrochemical measurements were tested on a CHI760E electrochemical workstation and Neware battery cycler (CT-4008T-5V50mA-164, Shenzhen, China). For electrode performances, the as-prepared electrode (1 cm × 1 cm) was directly used as the working electrode in a three-electrode configuration using 2 M KOH aqueous solution as the electrolyte, together with a platinum plate acting as the counter electrode and a saturated calomel electrode (SCE) as the reference electrode. Cyclic voltammetry (CV) tests were performed at a voltage window from 0 to 0.6 V and galvanostatic charging/discharging (GCD) tests were carried out at a voltage window from 0 to 0.5 V. The specific capacity could be calculated by the following equation:

$$C_s = I \times \Delta t/m \quad (1)$$

where C_s (C g^{-1}) was the specific capacity, I (A) was the discharge current, Δt (s) was the discharging time and m (g) was the mass of the active materials.

The electrocatalytic activity was also tested in a three-electrode configuration, where the electrolyte was changed to 1 M KOH. The polarization curves were measured by linear sweep voltammetry (LSV) at 10 mV s^{-1} for OER. All the potentials were calibrated to the reversible hydrogen electrode (RHE) by eqn (2). The Tafel slope was obtained by eqn (3).

$$E_{RHE} = E_{SCE} + 0.059pH + 0.197 \quad (2)$$

$$\eta = b \log j + a \quad (3)$$

where η is overpotential, b is the Tafel slope, j is the current density, and a is a constant.

For BSH devices, the electrochemical performances were tested in a two-electrode system. The BSH device was assembled by integrating NCNM core–shell nanoarrays as the positive electrode, the AC electrode as the negative electrode and 2 M KOH as the electrolyte together with the cellulose separator. (In order to make the electrode materials fully in contact with the electrolyte, the electrode was immersed in the electrolyte for at least 10 min in advance and then the device was assembled.) The power density (P, W kg^{-1}) and energy density (E, W h kg^{-1}) of the BSH could be calculated by the following equations:

$$C = I \times \Delta t/(m \times \Delta V) \quad (4)$$

$$E = C \times \Delta V^2/7.2 \quad (5)$$

$$P = 3600 \times E/\Delta t \quad (6)$$

where C (F g^{-1}) was the specific capacitance based on the total mass of the active materials of the positive electrode and the negative electrode (deducting the mass of the Ni foam substrate), ΔV (V) was the potential window, and Δt (s) was the discharging time. The charge balance between the two electrodes of the assembled BSH device is shown in the ESI.†

3. Results and discussion

3.1 Structural, morphological, and composition analysis

The synthetic strategy for the $NiCo_2O_4$ @ $NiMoO_4$ core–shell nanoarrays on nickel foam is schematically shown in Fig. 1 (see the Experimental section for details). First, different morphologies of $NiCo_2O_4$ nanoarrays were directly grown on the surface of Ni foams *via* a simple hydrothermal reaction. Next, $NiMoO_4$ nanosheets were coated onto the prepared Ni–Co precursors to form the core–shell nanostructure. After a thermal treatment in air at 450 °C, the porous samples could be obtained on NFs, which could be directly used as a working electrode for the application in both supercapacitors and electrocatalysis.

Scanning electron microscopy (SEM) images show that $NiCo_2O_4$@$NiMoO_4$ core–shell nanoarrays directly grew on the surface of NFs to form an interconnected 3D network (Fig. 2). As shown in Fig. 2a–d, densely packed NC-NW and NC-NS arrays both grew uniformly on Ni foam. The space between

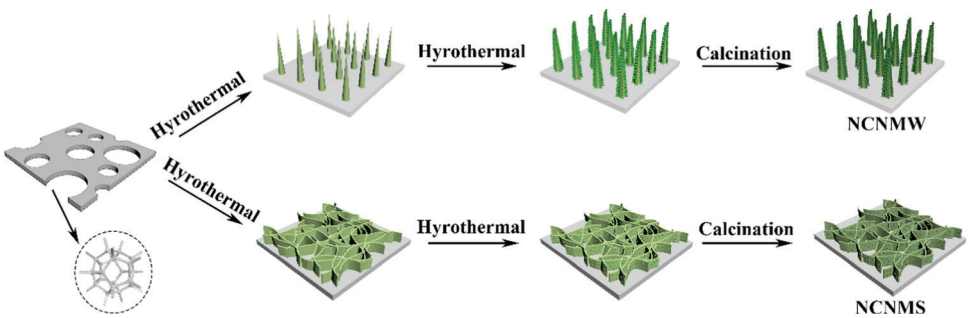

Fig. 1 Schematic illustration of the two-step synthesis process for $NiCo_2O_4$@$NiMoO_4$ core–shell nanostructure on Ni foam.

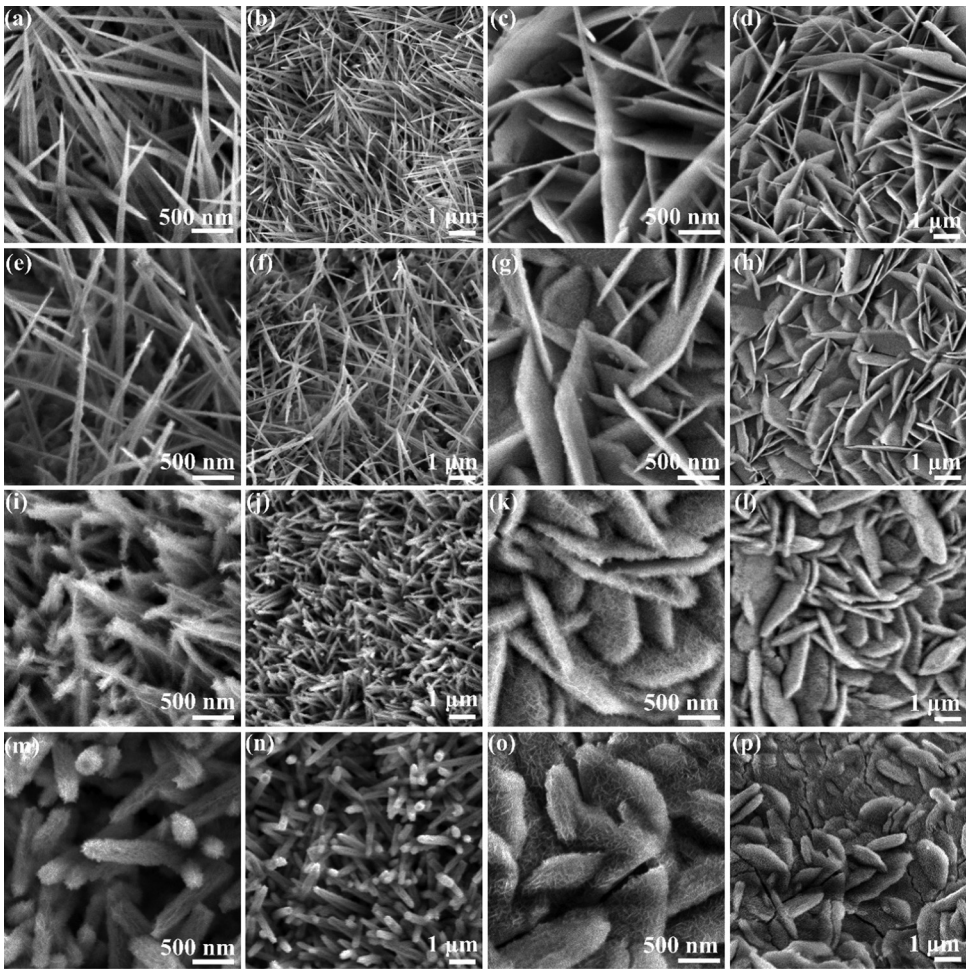

Fig. 2 SEM images of (a and b) NC-NW; (c and d) NC-NS; (e and f) NCNMW-1; (g and h) NCNMS-1; (i and j) NCNMW-2; (k and l) NCNMS-2; (m and n) NCNMW-3 and (o and p) NCNMS-3 nanoarrays on NFs.

nanowires (or nanosheets) could benefit the growth of $NiMoO_4$ nanosheets. When the reaction time of the synthesis of $NiMoO_4$ was 1 h, nanoparticles could be seen on the surface of the nanowires (or nanosheets), without any obvious nanosheet formation (as shown in Fig. 2e–h). As the reaction time progressed in the second step, the nanosheets gradually formed. As seen in Fig. 2i–l, when the reaction time was prolonged to 2 h, the $NiMoO_4$ nanosheet layer uniformly coated itself onto the surface of NC-NW and NC-NS, forming a core–shell nanostructure. In addition, the integration of the $NiMoO_4$ nanosheet layer on the NC-NW and NC-NS arrays did not destroy the original nanostructure. As shown in Fig. 2m–p, when the reaction time was 3 h, the $NiMoO_4$ nanosheet arrays were too thick and disordered. The thickness of the $NiMoO_4$ nanosheet caused the original structure to collapse and produced cracks, which hindered penetration of electrolyte. According to the results above, the reaction time in the second step reaction significantly affects the growth of $NiMoO_4$ nanosheets and can further affect the penetration of electrolyte and the electrochemical performances of the electrode, as discussed later.

The crystallographic structures of the prepared $NiCo_2O_4$@-$NiMoO_4$ core–shell nanostructure materials were characterized by XRD. The sample was scratched from NFs to exclude any influence from the Ni foam. As shown in Fig. 3a, the diffraction peaks (marked with "♦") located at 2θ values of 36.68°, 38.32°, 44.72°, 58.88° and 65.11° were attributed to the (311), (222), (400), (511) and (440) crystalline planes of the cubic spinel $NiCo_2O_4$ phase (ICDD card no. 20-0781), respectively. Meanwhile, the peaks marked "♥" at 31.14°, 31.21°, 52.22° and 55.24° were associated with the (111), (−111), (130) and (−202) planes of $NiMoO_4$ (ICDD card no. 16-0291), respectively. These observations confirm the presence of $NiCo_2O_4$ and $NiMoO_4$.

The surface composite and chemical valence states of each element were further investigated by XPS. The survey spectrum shown in Fig. 3b revealed the co-existence of Ni, Co, Mo and O. In the Ni 2p region (Fig. 3c), we attributed the peaks at 855.7 and 873.2 eV to the Ni $2p_{3/2}$ and Ni $2p_{1/2}$ peaks, respectively, with a spin-energy separation of 17.5 eV, because of spin–orbital effects. In addition, we observed two shake-up satellites at 880.6 and 861.9 eV (indicated as "Sat."), confirming the existence of Ni(II) in the NCNM.[40,41] The Co 2p spectrum (Fig. 3d) presented two main spin–orbital peaks (Co $2p_{3/2}$ and Co$2p_{1/2}$ at 780.5 eV and 796.2 eV, respectively, with a spin-energy separation of 15.7 eV), and two shakeup satellites (803.9

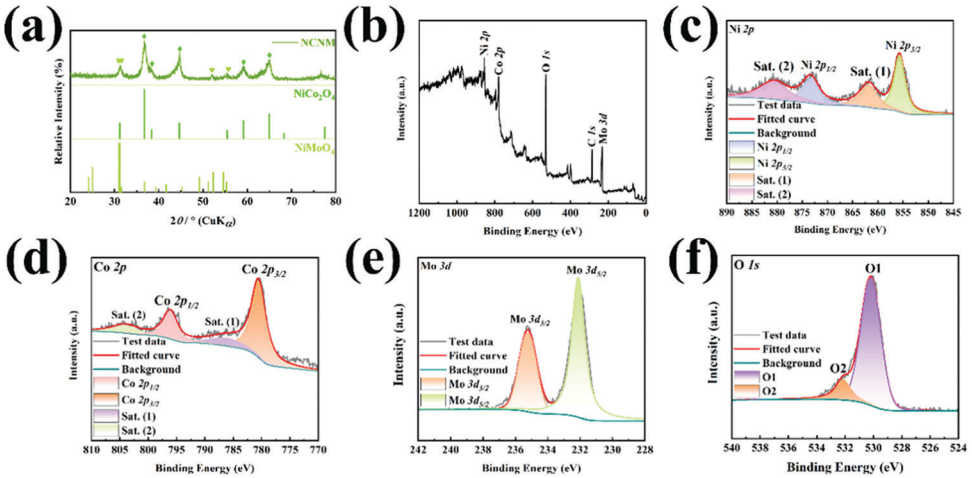

Fig. 3 (a) XRD pattern of core–shell nanostructured $NiCo_2O_4$@$NiMoO_4$ scratched from Ni foam. (b) Survey spectrum for NCNM composites. XPS spectra of (c) Ni 2p, (d) Co 2p, (e) Mo 3d, and (f) O 1s for $NiCo_2O_4$@$NiMoO_4$ core–shell nanoarrays.

and 786.5 eV), corresponding to the Co (III) oxidation state in the $NiCo_2O_4$.[41,42] Furthermore, the Mo 3d spectrum (Fig. 3e) showed two obvious peaks at 235.3 and 232.1 eV, with a spin-energy separation of 3.1 eV, which corresponded to Mo $3d_{3/2}$ and Mo $3d_{5/2}$, respectively, demonstrating the existence of the Mo^{6+} oxidation state in $NiMoO_4$.[31,41] The O 1s spectra in Fig. 3f could be fitted to two subpeaks: the peak at 530.1eV matched typical metal–oxygen bonds, and the peak at 532.2 eV corresponded to the absorbed water or water near the surface.[43–45] The results of XPS further confirmed the successful synthesis of the $NiCo_2O_4$@ $NiMoO_4$ core–shell nanostructure. Furthermore, the EDS results also confirmed the presence of each element found in the $NiCo_2O_4$@$NiMoO_4$ hierarchical nanostructure (Fig. S1, ESI†).

The unique architecture of NCNMS-2 and NCNMW-2 arrays were further confirmed through the use of TEM and HRTEM, as shown in Fig. 4. Fig. 4a and c show that the two kinds of Ni–Co precursors were both coated with a layer of nanosheets and formed two different core–shell nanostructures. In Fig. 4b and d, the HRTEM images of NCNMS-2 and NCNMW-2 both show that two different lattice spacings. In Fig. 4b, the lattice spacings of 0.233 nm and 0.168 nm were ascribed to the (222) plane of $NiCo_2O_4$ and the (−202) plane of $NiMoO_4$, respectively. In addition, the lattice spacings of 0.231 nm and 0.173 nm were ascribed to the (222) plane of $NiCo_2O_4$ and the (130) plane of $NiMoO_4$, respectively (as shown in Fig. 4d). These results correspond well with the XRD results. Moreover, the EDX spectroscopy mapping results in Fig. 4e and f show the homogeneous distributions of Ni, Co, Mo, and O for both NCNMS-2 and NCNMW-2, which agree with the results mentioned above. In short, the above results confirm successful synthesis of $NiCo_2O_4$@$NiMoO_4$ core–shell nanostructures.

3.2 Supercapacitor performance analysis

To evaluate the electrochemical properties of the prepared electrode, the electrode was first investigated as a supercapacitor electrode using a three-electrode system in 2 M KOH as the working electrode, together with an SCE as the reference electrode and a platinum plate as the counter electrode. Fig. 5a and b present the CV and GCD results of both NCNMS series composite electrodes and NCNMW series composite electrodes. The electrodes obtained from the two-hour hydrothermal process in the second step always demonstrated a better electrochemical performance (the details are shown in Table S1, ESI†) than those made from the one-hour or three-hour second hydrothermal process.

As the previous SEM images showed, the time of the second step reaction would affect the synthesis of the $NiMoO_4$ nanosheet layer, which could affect the penetration of the electrolyte. When the second hydrothermal procedure lasted an hour, insufficient electrochemical active sites existed because of insufficient loading of $NiMoO_4$ nanosheets. With regard to NCNMW-3 and NCNMS-3, the layer of the $NiMoO_4$ grew too thick, and cracks began to form. The thickness and cracks might impede the diffusion of electrolytes in the composite electrodes, leading to diminished electrochemical performance.

For comparison, we calculated the capacities from the GCD profiles recorded at a current density of 10 mA cm^{-2} in the potential window between 0 V and 0.5 V by using eqn (1). As mentioned earlier, the C_s of NCNMW-2 (1084.96 C g^{-1}), and NCNMS-2 (1656.33 C g^{-1}) were higher than their series electrodes (details shown in Table S1, ESI† and Fig. 5g). Additionally, the electrodes coated with $NiMoO_4$ exhibited much higher discharge time than the pure $NiCo_2O_4$ precursor electrodes. This further demonstrates that the synergetic effect of core and shell materials enhance the specific capacity of the electrode (as seen in Fig. S2b and S2c, ESI†). Therefore, we selected the NCNMW-2 and NCNMS-2 to form BSH devices for further electrochemical characterization.

The CV curves of NCNMW-2 and NCNMS-2 with a voltage window of 0–0.6 V at different scan rates (5–40 mV s^{-1}) are shown in Fig. 5c and e. A pair of sharp redox peaks appear in the CV curves, implying the existence of faradaic behavior

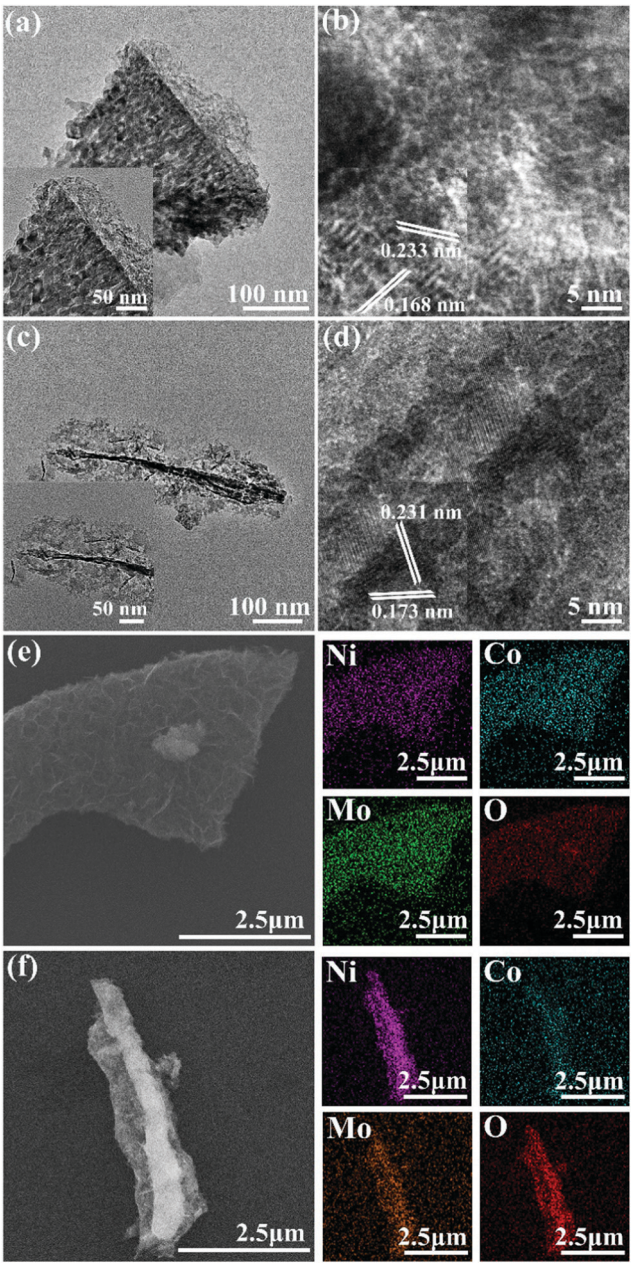

Fig. 4 TEM and HRTEM images of (a and b) NCNMS-2, and (c and d) NCNMW-2 scratched from Ni foam. EDS mapping of (e) NCNMS-2 nanostructure and (f) NCNMW-2 nanostructure.

during the electrochemical procedure. In addition, with an increasing scan rate, the CV curves retain their shape, indicating the desirable reversibility of the prepared electrodes.[38,46] The GCD curves of all prepared electrodes were nearly symmetric, without any significant IR drop, indicating the good reversibility of the as-prepared electrodes[47] (as shown in Fig. 5 and Fig. S3, ESI†).

Based on eqn (1), the NCNMS-2 electrode delivered high specific capacities of 1770.95 C g^{-1}, 1711.08 C g^{-1}, 1665.82 C g^{-1}, 1656.33 C g^{-1}, 1518.99 C g^{-1}, and 1334.18 C g^{-1} at a current density of 3 mA cm^{-2}, 5 mA cm^{-2}, 8 mA cm^{-2}, 10 mA cm^{-2}, 20 mA cm^{-2}, and 40 mA cm^{-2}, respectively (the records of NCNMW-2 are shown in Table S2, ESI†). We also measured the CV curves at various scan rates and the GCD curves at different current densities for NC-NW, NCNMW-1, NCNMW-3, NC-NS, NCNMS-1, and NCNMS-3 electrodes (Fig. S3, ESI†). The specific capacities of all electrodes are shown in Fig. S2b (ESI†) and Fig. 2c (the detailed results can be found in Table S1, ESI†). About 75.34% of the initial specific capacity of NCNMS-2 was retained even at a high current density of 40 mA cm^{-2}. The retention of initial specific capacity of NCNMS-2 was higher than those of NC-NW (39.68%), NCNMW-1 (41.16%), NCNMW-2 (64.08%), NCNMW-3 (45.15%), NC-NS (42.09%), NCNMS-1 (70.34%), and NCNMS-3 (70.93%). Due to its high value, NCNMS-2 had an excellent rate capability. In addition, the NCNMS-2 electrode possessed the lowest equivalent resistance of 0.82 Ω with regard to other electrodes (Fig. S2a and Table S1, ESI†).

To better elucidate the diffusion-controlled capacity and capacitance capacity in the electrochemical reaction processes, we applied kinetic analysis by obtaining the peak current (i) and scan rate (v) from the CV curves and evaluating the value of b according to eqn (7) and (8):[48,49]

$$i = av^b \quad (7)$$

$$\log i = b \log v + \log a \quad (8)$$

The value of b = 0.5 indicates a semi-infinite diffusion process, and b = 1 presents a capacitive process.[48] As shown in Fig. 5h, the calculated b value of NCNMW-2 and NCNMS-2 electrodes were calculated to be 0.59 for the anodic process and 0.56 and 0.57 for the cathodic process, respectively. These calculated values indicate NCNMW-2 and NCNMS-2 electrodes are similar to a battery-type material because they are close to 0.5. Additionally, the diffusion-controlled process contribution can be calculated from eqn (9) and (10):[50]

$$i(\mathrm{V}) = k_1 v + k_2 v^{1/2} \quad (9)$$

$$i(\mathrm{V})/v^{1/2} = k_1 v^{1/2} + k_2 \quad (10)$$

where, i(V) and v represent the current density and scan rate, respectively. Additionally, k_1 and k_2 are constants. Linear fitting of $i(\mathrm{V})/v^{1/2}$ and $v^{1/2}$ at different scan rates obtained k_1 and k_2. Fig. 5i shows that the capacitive contribution of NCNMS-2 was responsible for 9%, 12%, 13%, 15%, 17%, 18%, 20%, and 22% of the total current at scan rates of 5, 10, 15, 20, 25, 30, 35, and 40 mV s^{-1}, respectively (Fig. 5i). In addition, the capacitive contribution of NCNMW-2 was also recorded, as shown in Table S3 (ESI†). The overall contribution of the two electrodes is diffusion-controlled, which is consistent with the above results. Meanwhile, with increasing scan rates, the capacitive contribution of these two electrodes was enhanced since the high sweep rate inhibited the diffusion of ions. However, the capacitive processes were faster than faradaic processes and could cope with the increased scan rate,[51] further ensuring the excellent electrochemical properties of the electrodes.

Cycling stability is an important factor in determining the application of the electrodes in BSH devices. Fig. 5j presents the

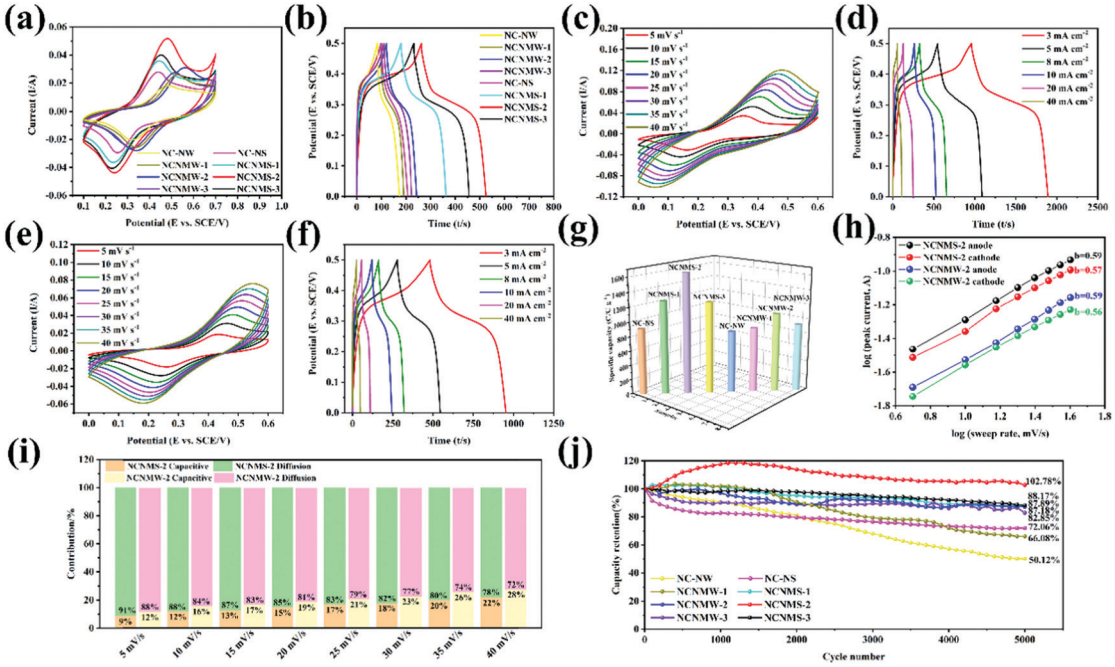

Fig. 5 (a) CV curves at 10 mV s^{-1}, and (b) GCD curves at 10 mA cm^{-2} of NC-NW, NCNMW-1, NCNMW-2, NCNMW-3, NC-NS, NCNMS-1, NCNMS-2 and NCNMS-3 electrodes. (c) CV curves of NCNMS-2 electrode at different scan rates; (d) GCD curves of NCNMS-2 electrode at different current densities; (e) CV curves of NCNMW-2 electrode at different scan rates; (f) GCD curves of NCNMW-2 electrode at different current densities; (g) specific capacity *versus* current density of NC-NW, NCNMW-1, NCNMW-2, NCNMW-3, NC-NS, NCNMS-1, NCNMS-2 and NCNMS-3 electrodes; (h) logarithmic relationship between the peak current and scan rates for NCNMW-2/NF and NCNMS-2/NF; (i) relative proportions of capacitive-controlled and diffusion-controlled contribution at various scanning rates for NCNMW-2/NF and NCNMS-2/NF; and (j) cycling performance of NC-NW, NCNMW-1, NCNMW-2, NCNMW-3, NC-NS, NCNMS-1, NCNMS-2 and NCNMS-3 electrodes.

cycling stability of all the prepared electrodes at a current density of 10 mA cm^{-2}. An excellent cycling behavior for the NCNMS-2 electrode with a capacity retention of 102.78% after 5000 charging/discharging cycles could be observed, which was higher than those of NC-NW (50.12%), NCNMW-1 (66.08%), NCNMW-2 (87.18%), NCNMW-3 (82.85%), NC-NS (72.06%), NCNMS-1 (87.89%) and NCNMS-3 (88.17%).

During the first 1400 cycles of NCNMS-2, the specific capacity significantly enhanced. There are two possible explanations for this observation. First, with the repeated penetration of electrolyte during the charging/discharging cycles, the surface wetting of the electrode could have improved.[52] Besides, the electrode could be activated creating more active sites for redox reactions during the cycles. In addition, after coating the electrode with $NiMoO_4$ nanosheets, the electrochemical properties improved in comparison to those of the pure $NiCo_2O_4$ nanostructure.

As a result, we attributed the excellent cycling stability of NCNMS-2 to a number of reasons. First, the stable nanostructure derived from the NC-NS allowed all nanosheets to support each other during the charging/discharging cycles. Second, after coating with $NiMoO_4$ layer, the original NC-NS could be protected, further ensuring the structural integrity of the NCNMS-2 electrode. Next, the core–shell nanostructure materials created more space for electrolyte penetration and had more active sites. As for the NC-NW electrode and the series electrodes, the nanowire structure could hardly accommodate the volume expansion due to the structural collapse during the cycles. Therefore, among all of the electrodes, the NCNMS-2 had the best cycling stability for use in BSH devices.

NCNMS-2 and NCNMW-2 electrodes had a high electrochemical performance in the corresponding series of electrodes. Therefore, the BSH devices included NCNMS-2 and NCNMW-2 electrodes as the positive electrodes, together with activated carbon as the negative electrode (named NCNMS-2//AC and NCNMW-2//AC). In addition, 2 M KOH served as the electrolyte in the design. Fig. 6a shows the CV curves of the assembled NCNMS-2//AC BSH device with different potential windows ranging from 0–1.0 V to 0–1.6 V at a scan rate of 10 mV s^{-1}. The figure fails to display evidence for polarization even when the voltage is enhanced to 1.6 V.

Additionally, the GCD curves of the NCNMS-2//AC device at a current density of 10 mA cm^{-2} in different potential ranges are displayed in Fig. 6b. The curves exhibit the same shape even at the potential windows of 1.6 V, indicating good capacitive performance. Therefore, we chose 1.6 V as the BSH device voltage to further evaluate the electrochemical performances.

Fig. 6c shows the CV curves of the fabricated NCNMS-2 BSH device in the voltage window of 0–1.6 V at various scan rates from 5 to 60 mV s^{-1}. All the CV curves showed a quasi-rectangular geometry, implying a capacitive behavior. Moreover, with increasing scan rates, the CV curves show slight peak shifts, which suggests the enhanced charge–discharge kinetics for the BSH device[1]. As shown in Fig. 6d, the GCD curves of the

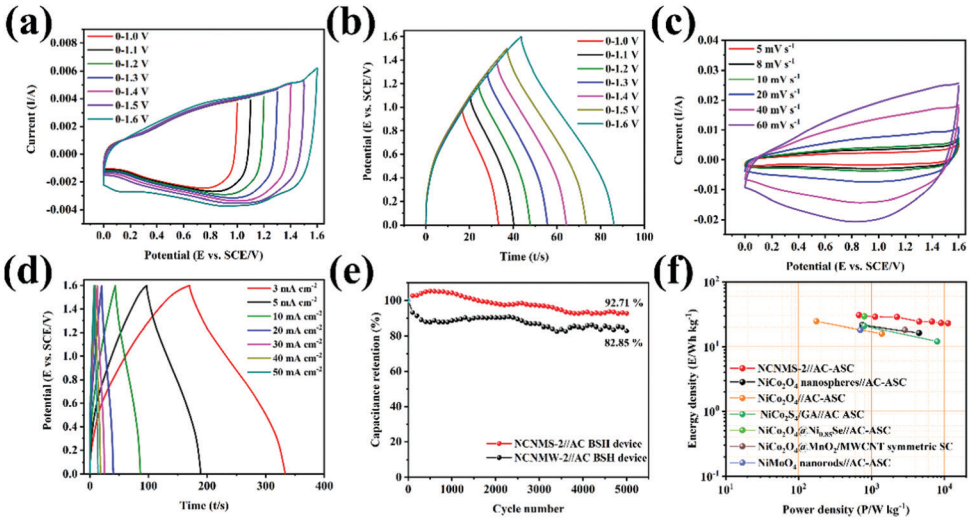

Fig. 6 (a) CV curves of the NCNMS-2//AC BSH device collected at different potential windows at a scan rate of 10 mV s^{-1}; (b) GCD curves of NCNMS-2//AC BSH device at a current density of 10 mA cm^{-2} with various potential windows; (c) CV curves of NCNMS-2//AC BSH device at different scan rates; (d) GCD curves at various current densities; (e) cycling performance of NCNMS-2//AC and NCNMW-2//AC BSH devices up to 5000 cycles; (f) Ragone plots (energy density *vs.* power density curves) of the BSH device.

NCNMS-2 BSH device retained symmetry when the voltage was up to 1.6 V, indicating the outstanding capacitive characteristics.[53] (The electrochemical performances of NCNMW-2//AC BSH device are shown in Fig. S4, ESI†)

The specific capacitances of these two BSH devices could be calculated from typical GCD curves at different currents using eqn (4). At an applied current density of 3 mA cm^{-2}, the NCNMS-2//AC device exhibited a high capacitance of 85.99 F g^{-1}. Moreover, at a large current density of 50 mA cm^{-2}, the BSH device still maintained a high capacitance of 64.26 F g^{-1}, showing a 74.73% capacitance retention of that at 3 mA cm^{-2}. Another important observance is how the capacitances of the NCNMW-2//AC BSH device were changed from 74.55 to 46.17 F g^{-1} at the current density ranging from 3 to 50 mA cm^{-2}, with a capacitance retention of 61.93%. The electrochemical properties of these two devices are shown in detail in Table S4 and Fig. S5 (ESI†).

Long-term cycling performance was carried out to further examine the cycling stability of the fabricated BSH devices. As shown in Fig. 6e, the electrochemical stability of these two BSH devices was evaluated at the current density of 10 mA cm^{-2} for 5000 cycles. The as-assembled NCNMS-2//AC BSH device retained 92.71% of its initial specific capacitance at a high current density of 10 mA cm^{-2} after 5000 cycles, which was higher than that of the NCNMW-2//AC BSH device (82.85% of its initial specific capacitance).

Energy/power densities are important factors to determine the practical applications of BSH devices. The energy density and power density were evaluated through the use of eqn (5) and (6). The calculated values were better than most of the previously reported supercapacitors, as shown in the Ragone plots of Fig. 6f. Remarkably, the fabricated NCNMS-2//AC BSH device could store a maximum energy density of 30.57 W h kg^{-1} at a power density of 676.06 W kg^{-1}. Even at a high-power density of 11 267.51 W kg^{-1}, the device still achieves an energy density of 22.85 W h kg^{-1}. The corresponding energy density and power density of this BSH device are much higher than those in some recently reported supercapacitor devices (Fig. 4h), such as $NiCo_2O_4$ nanospheres//AC,[54] $NiCo_2O_4$//AC-ASC,[55] $NiCo_2S_4$/GA//AC,[56] $NiCo_2O_4$@$Ni_{0.85}Se$//AC,[57] $NiCo_2O_4$@MnO_2/MWCNT-symmetric SC,[58] and $NiMoO_4$ nanorods//AC.[59] Based on the above records, the assembled NCNMS-2//AC BSH device and the NCNMW-2//AC BSH device exhibited high energy density and favorable cycling performance. Based on these results, they are promising candidates for potential applications in the area of energy storage devices.

3.3 Oxygen evolution reaction

As discussed above, the prepared electrodes could be used in the application of BSH devices. Furthermore, these electrodes are also found to be good catalysts for OER activity. All of the prepared materials were directly used as binder-free working electrodes for an electrocatalytic OER reaction, together with Ag/AgCl as the reference electrode and a platinum plate as the counter electrode in 1 M KOH (pH = 14) for a three-electrode system. The OER activities of the prepared electrodes were tested by linear sweep voltammetry (LSV), and the results are shown in Fig. 7. The voltage applied on the working electrode was linearly swept at a scan rate of 10 mV s^{-1} between 1.1 and 2.0 V (as against the reversible hydrogen electrode, RHE).

Fig. 7a shows the LSV curves of the prepared four electrodes. As shown in Fig. 7b, the overpotential at 10 mA cm^{-2} of NCNMS-2 was 175 mV, which was lower than that of NCNMW-2 (189 mV), NC-NS (253 mV), and NC-NW (320 mV), indicating acceptable OER activity for the NCNMS-2 electrode. Tafel analysis in Fig. 7c shows that the Tafel slope of NCNMS-2 is 59 mV dec^{-1}, which is smaller than those of NCNMW-2 (79 mV dec^{-1}), NC-NS (81 mV dec^{-1}), and NC-NW (88 mV dec^{-1}). These records further support how, after coating with a $NiMoO_4$

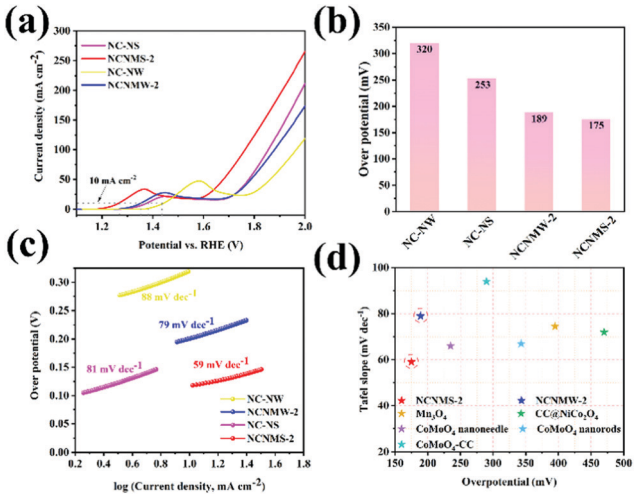

Fig. 7 (a) OER performance of NC-NS, NC-NW, NCNMS-2, and NCNMW-2 in a 1 M KOH electrolyte; (b) comparison of overpotential of NC-NS, NC-NW, NCNMS-2, and NCNMW-2 (at 10 mA cm^{-2}); (c) Tafel plots of different catalysts; (d) comparison between OER activity of NCNMS-2 and NCNMW-2 obtained herein (red circles indicate the overpotential and Tafel slope of current work) with those obtained previously.

nanosheet layer, the core–shell nanostructure materials enhanced OER kinetics and electrochemical properties. Furthermore, the OER activity reported herein was found to be much better than those reported previously (as shown in Fig. 7d).[37,60–63]

4. Conclusion

This paper reports the design and syntheses of hierarchical core–shell $NiCo_2O_4$@$NiMoO_4$ nanowires and nanosheets arrays directly on the Ni foam *via* a two-step controllable hydrothermal process. The synergistic effect between the $NiCo_2O_4$ core and the $NiMoO_4$ shell provides short ion diffusion length in addition to ample reaction sites. These merits enable them to be used as promising electrode materials for energy storage and electrocatalysis. In the supercapacitor, the NCNMS-2 electrode delivers a high specific capacity of 1770.95 C g^{-1} at a current density of 3 mA cm^{-2} and retains 102.78% capability retention after 5000 cycles at 10 mA cm^{-2}. Moreover, the BSH device with NCNMS-2 as the positive electrode and AC as the negative electrode yields a high energy density of 30.57 W h kg^{-1} at the power density of 676.06 W kg^{-1} and excellent stability with capacitance retention of 92.71% after 5000 continuous cycles at a current density of 10 mA cm^{-2}. As an electrocatalyst, the NCNMS-2 has excellent electrocatalytic activity for OER (an overpotential of 175 mV at 10 mA cm^{-2}) in 1 M KOH solution.

Considering both the simple preparation process and outstanding electrochemical properties, such novel electrode materials may have great potential for applications in both energy storage and electrocatalysis.

Conflicts of interest

There are no conflicts to declare.

Acknowledgements

This work was supported by the National Natural Science Foundation of China (No. 22171101) and the Open Fund Project of Key Laboratory of Electrochemical Energy Storage and Energy Conversion in Hainan Province of China (KFKT2019001).

References

1 D. Z. Kong, Y. Wang, S. Z. Huang, J. P. Hu, Y. Von Lim, B. Liu, S. Fan, Y. M. Shi and H. Y. Yang, 3D self-branched zinc-cobalt Oxide@N-doped carbon hollow nanowall arrays for high-performance asymmetric supercapacitors and oxygen electrocatalysis, *Energy Storage Mater.*, 2019, **23**, 653–663.

2 W. Du, Y. L. Bai, J. Q. Xu, H. B. Zhao, L. Zhang, X. F. Li and J. J. Zhang, Advanced metal-organic frameworks (MOFs) and their derived electrode materials for supercapacitors, *J. Power Sources*, 2018, **402**, 281–295.

3 Z. W. Seh, J. Kibsgaard, C. F. Dickens, I. B. Chorkendorff, J. K. Norskov and T. F. Jaramillo, Combining theory and experiment in electrocatalysis: Insights into materials design, *Science*, 2017, **355**, 6321.

4 J. Yang, C. D. Wang, H. X. Ju, Y. Sun, S. Q. Xing, J. F. Zhu and Q. Yang, Integrated Quasiplane Heteronanostructures of $MoSe_2/Bi_2Se_3$ Hexagonal Nanosheets: Synergetic Electrocatalytic Water Splitting and Enhanced Supercapacitor Performance, *Adv. Funct. Mater.*, 2017, **27**, 48.

5 X. Y. Yu and X. W. Lou, Mixed Metal Sulfides for Electrochemical Energy Storage and Conversion, *Adv. Energy Mater.*, 2018, **8**, 3.

6 T. Kwon, H. Hwang, Y. J. Sa, J. Park, H. Baik, S. H. Joo and K. Lee, Cobalt Assisted Synthesis of IrCu Hollow Octahedral Nanocages as Highly Active Electrocatalysts toward Oxygen Evolution Reaction, *Adv. Funct. Mater.*, 2017, **27**, 7.

7 M. S. Balogun, Y. C. Huang, W. T. Qiu, H. Yang, H. B. Ji and Y. X. Tong, Updates on the development of nanostructured transition metal nitrides for electrochemical energy storage and water splitting, *Mater. Today*, 2017, **20**(8), 425–451.

8 H. C. Tang, Y. H. Yuan, L. Meng, W. C. Wang, J. G. Lu, Y. J. Zeng, T. Q. Huang and C. Gao, Low-Resistance Porous Nanocellular MnSe Electrodes for High-Performance All-Solid-State Battery-Supercapacitor Hybrid Devices, *Adv. Mater. Technol.*, 2018, **3**, 7.

9 D. Z. Kong, Y. Wang, Y. Von Lim, S. Z. Huang, J. Zhang, B. Liu, T. P. Chen and H. Y. Yang, 3D hierarchical defect-rich $NiMo_3S_4$ nanosheet arrays grown on carbon textiles for high-performance sodium-ion batteries and hydrogen evolution reaction, *Nano Energy*, 2018, **49**, 460–470.

10 T. Chen, S. Z. Li, J. Wen, P. B. Gui, Y. X. Guo, C. Guan, J. P. Liu and G. J. Fang, Rational Construction of Hollow Core-Branch $CoSe_2$ Nanoarrays for High-Performance Asymmetric Supercapacitor and Efficient Oxygen Evolution, *Small*, 2018, **14**, 5.

11 J. Zhao, Z. J. Li, X. C. Yuan, Z. Yang, M. Zhang, A. Meng and Q. D. Li, A High-Energy Density Asymmetric Supercapacitor Based on Fe_2O_3 Nanoneedle Arrays and $NiCo_2O_4$/$Ni(OH)_2$ Hybrid Nanosheet Arrays Grown on SiC Nanowire Networks as Free-Standing Advanced Electrodes, *Adv. Energy Mater.*, 2018, **8**, 12.

12 N. L. W. Septiani, Y. V. Kaneti, K. B. Fathoni, J. Wang, Y. Ide, B. Yuliarto, Nugraha, H. K. Dipojono, A. K. Nanjundan, D. Golberg, Y. Bando and Y. Yamauchi, Self-assembly of nickel phosphate-based nanotubes into two-dimensional crumpled sheet-like architectures for high-performance asymmetric supercapacitors, *Nano Energy*, 2020, 67.

13 J. Tang, R. R. Salunkhe, H. B. Zhang, V. Malgras, T. Ahamad, S. M. Alshehri, N. Kobayashi, S. Tominaka, Y. Ide, J. H. Kim and Y. Yamauchi, Bimetallic Metal-Organic Frameworks for Controlled Catalytic Graphitization of Nanoporous Carbons, *Sci. Rep.*, 2016, 6.

14 Y. Li, J. Henzie, T. Park, J. Wang, C. Young, H. Q. Xie, J. W. Yi, J. Li, M. Kim, J. Kim, Y. Yamauchi and J. Na, Fabrication of Flexible Microsupercapacitors with Binder-Free ZIF-8 Derived Carbon Films via Electrophoretic Deposition, *Bull. Chem. Soc. Jpn.*, 2020, **93**(1), 176–181.

15 X. T. Xu, J. Tang, H. Y. Qian, S. J. Hou, Y. Bando, M. S. A. Hossain, L. K. Pan and Y. Yamauchi, Three-Dimensional Networked Metal-Organic Frameworks with Conductive Polypyrrole Tubes for Flexible Supercapacitors, *ACS Appl. Mater. Interfaces*, 2017, **9**(44), 38737–38744.

16 A. Azhar, Y. C. Li, Z. X. Cai, M. B. Zakaria, M. K. Masud, M. S. A. Hossain, J. Kim, W. Zhang, J. Na, Y. Yamauchi and M. Hu, Nanoarchitectonics: A New Materials Horizon for Prussian Blue and Its Analogues, *Bull. Chem. Soc. Jpn.*, 2019, **92**(4), 875–904.

17 H. B. Wu, H. Pang and X. W. Lou, Facile synthesis of mesoporous $Ni_{0.3}Co_{2.7}O_4$ hierarchical structures for high-performance supercapacitors, *Energy Environ. Sci.*, 2013, **6**(12), 3619–3626.

18 Y. Y. Liang, H. L. Wang, J. G. Zhou, Y. G. Li, J. Wang, T. Regier and H. J. Dai, Covalent Hybrid of Spinel Manganese-Cobalt Oxide and Graphene as Advanced Oxygen Reduction Electrocatalysts, *J. Am. Chem. Soc.*, 2012, **134**(7), 3517–3523.

19 Y. Gao, L. W. Mi, W. T. Wei, S. Z. Cui, Z. Zheng, H. W. Hou and W. H. Chen, Double Metal Ions Synergistic Effect in Hierarchical Multiple Sulfide Microflowers for Enhanced Supercapacitor Performance, *ACS Appl. Mater. Interfaces*, 2015, **7**(7), 4311–4319.

20 X. H. Qi, W. J. Zheng, G. H. He, T. F. Tian, N. X. Du and L. Wang, $NiCo_2O_4$ hollow microspheres with tunable numbers and thickness of shell for supercapacitors, *Chem. Eng. J.*, 2017, **309**, 426–434.

21 P. Peng, X. M. Lin, Y. Z. Liu, A. S. Filatov, D. G. Li, V. R. Stamenkovic, D. L. Yang, V. B. Prakapenka, A. W. Lei and E. V. Shevchenko, Binary Transition-Metal Oxide Hollow Nanoparticles for Oxygen Evolution Reaction, *ACS Appl. Mater. Interfaces*, 2018, **10**(29), 24715–24724.

22 W. H. Zuo, C. Y. Xie, P. Xu, Y. Y. Li and J. P. Liu, A Novel Phase-Transformation Activation Process toward Ni-Mn-O Nanoprism Arrays for 2.4 V Ultrahigh-Voltage Aqueous Supercapacitors, *Adv. Mater.*, 2017, **29**, 36.

23 N. T. Suen, S. F. Hung, Q. Quan, N. Zhang, Y. J. Xu and H. M. Chen, Electrocatalysis for the oxygen evolution reaction: recent development and future perspectives, *Chem. Soc. Rev.*, 2017, **46**(2), 337–365.

24 L. Yu, B. Y. Guan, W. Xiao and X. W. Lou, Formation of Yolk-Shelled Ni-Co Mixed Oxide Nanoprisms with Enhanced Electrochemical Performance for Hybrid Supercapacitors and Lithium Ion Batteries, *Adv. Energy Mater.*, 2015, **5**, 21.

25 C. Wang, J. Y. Wang, W. P. Hu and D. Wang, Controllable Synthesis of Hollow Multishell Structured Co_3O_4 with Improved Rate Performance and Cyclic Stability for Supercapacitors, *Chem. Res. Chin. Univ.*, 2020, **36**(1), 68–73.

26 L. F. Hu, L. M. Wu, M. Y. Liao, X. H. Hu and X. S. Fang, Electrical Transport Properties of Large, Individual $NiCo_2O_4$ Nanoplates, *Adv. Funct. Mater.*, 2012, **22**(5), 998–1004.

27 K. W. Qiu, Y. Lu, D. Y. Zhang, J. B. Cheng, L. Yan, J. Y. Xu, X. M. Liu, J. K. Kim and Y. S. Luo, Mesoporous, hierarchical core/shell structured $ZnCo_2O_4$/MnO_2 nanocone forests for high-performance supercapacitors, *Nano Energy*, 2015, **11**, 687–696.

28 J. Bao, Z. L. Wang, W. J. Liu, L. Xu, F. C. Lei, J. F. Xie, Y. Zhao, Y. P. Huang, M. L. Guan and H. M. Li, $ZnCo_2O_4$ ultrathin nanosheets towards the high performance of flexible supercapacitors and bifunctional electrocatalysis, *J. Alloys Compd.*, 2018, **764**, 565–573.

29 Y. Q. Wang, D. W. Yang, J. N. Lian, T. Wei and Y. M. Sun, Ordered corn-like $CuCo_2O_4$ nanoforests covering Ni foam for a high-performance all-solid-state supercapacitor, *J. Alloys Compd.*, 2018, **741**, 527–531.

30 K. Zhang, W. Zeng, G. Zhang, S. Hou, F. Wang, T. Wang and H. Duan, Hierarchical $CuCo_2O_4$ nanowire@$NiCo_2O_4$ nanosheet core/shell arrays for high-performance supercapacitors, *RSC Adv.*, 2015, **5**(85), 69636–69641.

31 V. S. Budhiraju, A. Sharma and S. Sivakumar, Structurally Stable Mesoporous Hierarchical $NiMoO_4$ Hollow Nanofibers for Asymmetric Supercapacitors with Enhanced Capacity and Improved Cycling Stability, *ChemElectroChem*, 2017, **4**(12), 3331–3339.

32 G. M. Tomboc and H. Kim, Highly porous $NiMoO_4$ tailored onto amine functionalized CNT as advanced nanocomposite electrocatalyst for supercapacitor application, *J. Mater. Sci.: Mater. Electron.*, 2019, **30**(10), 9558–9571.

33 F. Yang, J. Chu, Y. P. Cheng, J. F. Gong, X. Q. Wang and S. X. Xiong, Hydrothermal Synthesis of NiCo-layered Double Hydroxide Nanosheets Decorated on Biomass Carbon Skeleton for High Performance Supercapacitor, *Chem. Res. Chin. Univ.*, 2021, **37**(3), 772–777.

34 C. X. Chen, C. Y. Zhao, C. H. Li, J. H. Liu and D. Y. Gui, Porous $NiCo_2O_4$ Nanowire Arrays as Supercapacitor Electrode Materials with Extremely High Cycling Stability, *Chem. Res. Chin. Univ.*, 2020, **36**(4), 715–720.

35 Q. Zhou, S. Z. Jiao, B. Zheng and Z. Y. Li, Preparation and Pseudo-capacitance Performance of $NiCo_2O_4$ Nanosheets, *Chem. Res. Chin. Univ.*, 2019, **35**(6), 957–961.

36 S. Kumar, G. Saeed, N. H. Kim and J. H. Lee, Hierarchical nanohoneycomb-like $CoMoO_4$-MnO_2 core-shell and Fe_2O_3 nanosheet arrays on 3D graphene foam with excellent supercapacitive performance, *J. Mater. Chem. A*, 2018, **6**(16), 7182–7193.

37 L. X. Fang, F. Wang, T. L. Zhai, Y. Qiu, M. D. Lan, K. J. Huang and Q. S. Jing, Hierarchical $CoMoO_4$ nanoneedle electrodes for advanced supercapacitors and electrocatalytic oxygen evolution, *Electrochim. Acta*, 2018, **259**, 552–558.

38 W. J. Chu, Z. J. Shi, Y. D. Hou, D. N. Ma, X. Bai, Y. F. Gao and N. J. Yang, Trifunctional of Phosphorus-Doped $NiCo_2O_4$ Nanowire Materials for Asymmetric Supercapacitor, Oxygen Evolution Reaction, and Hydrogen Evolution Reaction, *ACS Appl. Mater. Interfaces*, 2020, **12**(2), 2763–2772.

39 S. D. Raut, H. R. Mane, N. M. Shinde, D. Lee, S. F. Shaikh, K. H. Kim, H. J. Kim, A. M. Al-Enizi and R. S. Mane, Electrochemically grown MnO_2 nanowires for supercapacitor and electrocatalysis applications, *New J. Chem.*, 2020, **44**(41), 17864–17870.

40 C. Chen, D. Yan, X. Luo, W. Gao, G. Huang, Z. Han, Y. Zeng and Z. Zhu, Construction of Core-Shell $NiMoO_4$@Ni-Co-S Nanorods as Advanced Electrodes for High-Performance Asymmetric Supercapacitors, *ACS Appl. Mater. Interfaces*, 2018, **10**(5), 4662–4671.

41 J. F. Moulder, W. F. Stickle, P. E. Sobol and K. D. J. P.-E. C. Bomben, *Handbook of X-ray Photoelectron Spectroscopy*, Eden Prairie, MN, Chastain, J. 1992.

42 M. T. Saray and H. Hosseini, Mesoporous MnNi-CoO_4@MnO_2 core-shell nanowire/nanosheet arrays on flexible carbon cloth for high-performance supercapacitors, *Electrochim. Acta*, 2016, **222**, 505–517.

43 A. K. Tomar, G. Singh and R. K. Sharma, Fabrication of a Mo-Doped Strontium Cobaltite Perovskite Hybrid Supercapacitor Cell with High Energy Density and Excellent Cycling Life, *ChemSusChem*, 2018, **11**(23), 4123–4130.

44 N. Wang, B. L. Sun, P. Zhao, M. Q. Yao, W. C. Hu and S. Komarneni, Electrodeposition preparation of $NiCo_2O_4$ mesoporous film on ultrafine nickel wire for flexible asymmetric supercapacitors, *Chem. Eng. J.*, 2018, **345**, 31–38.

45 Y. Y. Dong, Y. Wang, Y. N. Xu, C. C. Chen, Y. J. Wang, L. F. Jiao and H. T. Yuan, Facile synthesis of hierarchical nanocage $MnCo_2O_4$ for high performance supercapacitor, *Electrochim. Acta*, 2017, **225**, 39–46.

46 X. W. Dong, Y. Y. Zhang, W. J. Wang and R. Zhao, Rational construction of 3D $NiCo_2O_4$@$CoMoO_4$ core/shell nanoarrays as a positive electrode for asymmetric supercapacitor, *J. Alloys Compd.*, 2017, **729**, 716–723.

47 P. X. Li, C. H. Ruan, J. Xu and Y. B. Xie, A high-performance asymmetric supercapacitor electrode based on a three-dimensional $ZnMoO_4$/CoO nanohybrid on nickel foam, *Nanoscale*, 2019, **11**(28), 13639–13649.

48 Y. L. Zhu, Q. Zong, Q. L. Zhang, H. Yang, Q. Q. Wang and H. Y. Wang, Three-dimensional core-shell NiCoP@NiCoP array on carbon cloth for high performance flexible asymmetric supercapacitor, *Electrochim. Acta*, 2019, **299**, 441–450.

49 V. Augustyn, P. Simon and B. Dunn, Pseudocapacitive oxide materials for high-rate electrochemical energy storage, *Energy Environ. Sci.*, 2014, **7**(5), 1597–1614.

50 N. Deka, J. Barman, P. Gawas, H. B. Parse, B. Kakade, V. Nutalapati and G. K. Dutta, Nitrogen-Doped Microporous Carbons Synthesized from IndoleBased Copolymer Spheres for Supercapacitors and Metal-Free Electrocatalysis, *Energy Fuels*, 2021, **35**(3), 2785–2794.

51 A. M. Huang, Q. Q. Wang, Z. Y. Ma, K. Rui, X. Huang, J. X. Zhu and W. Huang, Surface Anionization of Self-Assembled Iron Sulfide Hierarchitectures to Enhance Capacitive Storage for Alkaline -Metal Ion Batteries, *ACS Appl. Mater. Interfaces*, 2019, **11**(43), 39991–39997.

52 G. J. He, J. M. Li, W. Y. Li, B. Li, N. Noor, K. B. Xu, J. Q. Hu and I. P. Parkin, One pot synthesis of nickel foam supported self-assembly of $NiWO_4$ and $CoWO_4$ nanostructures that act as high performance electrochemical capacitor electrodes, *J. Mater. Chem. A*, 2015, **3**(27), 14272–14278.

53 J. S. Lin, L. Yao, Z. L. Li, P. X. Zhang, W. H. Zhong, Q. H. Yuan and L. B. Deng, Hybrid hollow spheres of carbon@$Co_xNi_{1-x}MoO_4$ as advanced electrodes for high-performance asymmetric supercapacitors, *Nanoscale*, 2019, **11**(7), 3281–3291.

54 K. B. Xu, J. M. Yang and J. Q. Hu, Synthesis of hollow $NiCo_2O_4$ nanospheres with large specific surface area for asymmetric supercapacitors, *J. Colloid Interface Sci.*, 2018, **511**, 456–462.

55 J. Bhagwan, G. Nagaraju, B. Ramulu, S. C. Sekhar and J. S. Yu, Rapid synthesis of hexagonal $NiCo_2O_4$ nanostructures for high-performance asymmetric supercapacitors, *Electrochim. Acta*, 2019, **299**, 509–517.

56 B. X. Li, Z. Tian, H. J. Li, Z. W. Yang, Y. Z. Wang and X. M. Wang, Self-supporting graphene aerogel electrode intensified by $NiCo_2S_4$ nanoparticles for asymmetric supercapacitor, *Electrochim. Acta*, 2019, **314**, 32–39.

57 Y. W. Sui, A. Ye, J. Q. Qi, F. X. Wei, Y. Z. He, Q. K. Meng, Y. J. Ren and Z. Sun, Construction of $NiCo_2O_4$@$Ni_{0.85}Se$ core-shell nanorod arrays on Ni foam as advanced materials for an asymmetric supercapacitor, *J. Alloys Compd.*, 2019, **778**, 234–238.

58 S. Karmakar, R. Boddhula, B. Sahoo, B. Raviteja and D. Behera, Electrochemical performance of heterogeneous, mesopores and non-centrosymmetric Core@shell $NiCo_2O_4$@MnO_2 nanocomposites and its MWCNT blended complex for supercapacitor applications, *J. Solid State Chem.*, 2019, **280**, 221–230.

59 N. S. Neeraj, B. Mordina, A. K. Srivastava, K. Mukhopadhyay and N. E. Prasad, Impact of process conditions on the electrochemical performances of $NiMoO_4$ nanorods and activated carbon based asymmetric supercapacitor, *Appl. Surf. Sci.*, 2019, **473**, 807–819.

60 K. H. Cho, H. Seo, S. Park, Y. H. Lee, M. Y. Lee, N. H. Cho and K. T. Nam, Uniform, Assembled 4 nm Mn_3O_4

Nanoparticles as Efficient Water Oxidation Electrocatalysts at Neutral pH, *Adv. Funct. Mater.*, 2020, **30**, 10.

61 C. Guan, X. M. Liu, W. N. Ren, X. Li, C. W. Cheng and J. Wang, Rational Design of Metal-Organic Framework Derived Hollow $NiCo_2O_4$ Arrays for Flexible Supercapacitor and Electrocatalysis, *Adv. Energy Mater.*, 2017, **7**, 12.

62 X. L. Liu, Y. X. Yang and S. Y. Guan, An efficient electrode based on one-dimensional $CoMoO_4$ nanorods for oxygen evolution reaction, *Chem. Phys. Lett.*, 2017, **675**, 11–14.

63 J. L. Meng, J. Q. Fu, X. X. Yang, M. J. Wei, S. Liang, H. Y. Zang, H. Q. Tan, Y. H. Wang and Y. G. Li, Efficient $MMoO_4$ (M = Co, Ni) carbon cloth electrodes for water oxidation, *Inorg. Chem. Front.*, 2017, **4**(11), 1791–1797.